How model uncertainties influence tropical humidity in global storm-resolving simulations

Theresa Lang[1,2], Ann Kristin Naumann[3,1], Stefan A. Buehler[1], Bjorn Stevens[3], Hauke Schmidt[3], Franziska Aemisegger[4],

[1]Meteorological Institute, Center for Earth System Research and Sustainability (CEN), Universität Hamburg, Hamburg, Germany
[2]International Max Planck Research School on Earth System Modelling, Max Planck Institute for Meteorology, Hamburg, Germany
[3]Max Planck Institute for Meteorology, Hamburg, Germany
[4]Institute for Atmospheric and Climate Science, ETH Zurich, Zurich, Switzerland

Key Points:

- Sensitivity experiments suggest that parameterizations are the major source of relative humidity spread across global storm-resolving models
- Vertical mixing processes strongly impact the humidity of the moist tropics by affecting last-saturation statistics within the tropics
- The humidity of the dry tropics is disproportionately sensitive to changes in the pathways of exchange with the extra-tropics

Corresponding author: Theresa Lang, theresa.lang@uni-hamburg.de

Abstract

We conduct a series of eight 45-day experiments with a global storm-resolving model (GSRM) to test the sensitivity of relative humidity $\mathcal{R}$ in the tropics to changes in model resolution and parameterizations. These changes include changes in horizontal and vertical grid spacing as well as in the parameterizations of microphysics and turbulence, and are chosen to capture currently existing differences among GSRMs. To link the $\mathcal{R}$ distribution in the tropical free troposphere with processes in the deep convective regions, we adopt a trajectory-based assessment of the last-saturation paradigm. The perturbations we apply to the model result in tropical mean $\mathcal{R}$ changes ranging from 0.5% to 8% (absolute) in the mid troposphere. The generated $\mathcal{R}$ spread is similar to that in a multi-model ensemble of GSRMs and smaller than the spread across conventional general circulation models, supporting that an explicit representation of deep convection reduces the uncertainty in tropical $\mathcal{R}$. The largest $\mathcal{R}$ changes result from changes in parameterizations, suggesting that model physics represent a major source of humidity spread across GSRMs. The $\mathcal{R}$ in the moist tropical regions is disproportionately sensitive to vertical mixing processes within the tropics, which impact $\mathcal{R}$ through their effect on the last-saturation temperature rather than their effect on the evolution of the humidity since last-saturation. In our analysis the $\mathcal{R}$ of the dry tropical regions strongly depends on the exchange with the extra-tropics. The interaction between tropics and extratropics could change with warming and presage changes in the radiatively sensitive dry regions.

Plain Language Summary

Water vapor is the most important greenhouse gas in the atmosphere. Therefore, for the prediction of future warming it is important that climate models capture the distribution of atmospheric humidity and its change under warming. However, climate models currently strongly disagree in their representation of humidity, causing uncertainty in climate predictions. A recent study has shown that, while there is better agreement among the newest generation of climate models, so called global storm-resolving models, the remaining inter-model differences are still relevant and therefore need to be better understood. To narrow down the causes of these differences, in this study we examine how much the humidity in a storm-resolving model changes in response to changes in different model components, which are chosen to reflect the differences that currently exist between models. We find the largest humidity changes in response to changes in the model's representation of sub-grid scale processes. In storm-resolving models these are turbulent motions and cloud microphysics. Our results suggest that differences in the representation of these processes cause a major part of the humidity differences between storm-resolving models.

1 Introduction

The aim of this study is to better understand sources of uncertainties in modelling processes that drive the distribution of tropical free-tropospheric relative humidity. Therefore, we examine how much and through which physical mechanisms the relative humidity in a global storm-resolving model (GSRM) – the newest generation of climate models with high horizontal resolution and explicit simulation of convection – is affected by changes in model resolution and paramtererizations.

Free-tropospheric relative humidity plays an important role in determining Earth's climate sensitivity. The combined effect of the water vapor and lapse rate feedbacks – the two most important feedbacks acting under clear-sky conditions – largely depends on how relative humidity responds to warming (Held & Shell, 2012). While to first order relative humidity is expected to stay constant under warming (Held & Soden, 2000), even small deviations from this constancy significantly impact the clear-sky feedback by

altering the cancellation between water vapor and lapse rate feedbacks in the saturated parts of the emission spectrum (Bony et al., 2006). In line with that, model differences in the relative humidity response control the prevailing spread in clear-sky feedback across general circulation models (GCMs; Vial et al., 2013). Since the relative humidity change simulated by GCMs is described by an upward shift following the rising isotherms, differences in the models' relative humidity response are closely related to differences in their climatology (Po-Chedley et al., 2019). Even if relative humidity does not change with warming, its present-day value might affect the clear-sky feedback. While no systematic relationship between present-day state and feedbacks has been found for GCMs (John & Soden, 2007), 1D radiative convective equilibrium (RCE) studies suggest that particularly at high surface temperatures characteristic of the tropics, the closing of the spectral window results in a strong dependence of the clear-sky feedback on relative humidity (Kluft et al., 2019; Bourdin et al., 2021; McKim et al., 2021). Thus, to develop a more fundamental understanding of climate and climate change, we will need to understand what sets the distribution of relative humidity, how it might change, and why it differs across models.

The sources of the relative humidity spread across models are poorly understood. One reason for this is the number of processes that affect humidity, many of which are poorly constrained in GCMs. In particular deep convection, the process accounting for most of the vertical transport of water vapour in the tropical atmosphere, is not resolved in these models and needs to be parameterized. An important step has been made with the development of global storm-resolving models (GSRMs; Satoh et al., 2019). With grid spacings of a few kilometers, these models simulate deep convection explicitly and thereby forego the need for convective parameterizations. At present, due to the high computational effort, storm-resolving simulations are limited to time scales of days to months. A first intercomparison of GSRMs, the DYnamics of the Atmospheric general circulation Modeled On Non-hydrostatic Domains (DYAMOND; Stevens et al., 2019) project, indicates that the inter-model spread in tropical free-tropospheric humidity is indeed reduced compared to GCMs (Lang et al., 2021). While this is a promising result and highlights the benefit of even approximately resolving deep convection, the study also showed that the remaining differences in relative humidity are still an important source of uncertainty for the clear-sky outgoing longwave radiation (OLR).

In this study, we attempt to understand the reasons behind the remaining relative humidity differences. To this end, we examine how the tropical humidity simulated by a GSRM changes in response to modifications in model resolution and model physics. These modifications are chosen to resemble currently existing differences across GSRMs. A large ensemble of back-trajectories started from the tropical mid troposphere allows us to examine the history of the air parcels arriving in these regions and hence the physical mechanisms behind humidity changes in the experiments.

To examine these mechanisms we make use of the last-saturation or advection-condensation paradigm (Sherwood, 1996; Sherwood et al., 2010), which represents the simplest model of what determines the distribution of free-tropospheric humidity. Assuming that water vapor behaves as a conservative tracer for which condensation is a permanent sink term, the water vapor content of an air parcel is determined by its temperature at the instant at which condensation last occurred. Inside a cloud, an air parcel's specific humidity is at saturation. As the parcel rises, it looses water vapor by condensation. Outside the cloud, the air parcel subsides and warms adiabatically, while maintaining the specific humidity it had when it was last saturated, so its relative humidity decreases. The regions where last-condensation events typically occur are often referred to as the "source regions" or "origins" of free-tropospheric air. The source regions of tropical free-

tropospheric air are mainly located in the tropical deep convective regions, but a significant part of the air in the dry subtropical subsidence regions also originates from the extra-tropics (e.g. Cau et al., 2007; Roca et al., 2012; Aemisegger et al., 2021). According to the last-saturation model, the relative humidity in a given target region only depends on the properties – mainly the temperature – of the source region and the target region.

Numerical implementations of the last-saturation model, which used large-scale wind and temperature fields from meteorological analyses to calculate Lagrangian back-trajectories, have been successful in reproducing the observed free-tropospheric relative humidity distribution (e.g. Sherwood, 1996; Pierrehumbert & Roca, 1998; Dessler & Sherwood, 2000). This has lead to the conclusion that the relative humidity distribution is determined by circulation and temperature structure, while any moisture sources or sinks changing the specific humidity of an air parcel after the last-saturation event are of minor importance. These sources and sinks include evaporation of cloud condensate or from precipitation, as well as mixing due to motions on scales not resolved in the wind field used for the trajectory calculation. This is not to say that these processes are unimportant, rather to say that to the extent they are important, it is through their indirect influence on the atmospheric circulation and the temperature structure, which ultimately determine the location of last-saturation events.

While the moisture sources and sinks after last-saturation appear to play a secondary role in determining spatial variations of relative humidity in the real atmosphere or a given model, it is less clear whether they might be important when it comes to explaining the more subtle humidity differences between models, particularly when different parameterizations for the processes causing the sources and sinks, i.e. microphysics and turbulence, are used. To test this, we calculate back-trajectories to perform two types of Lagrangian relative humidity reconstructions for our model experiments. The first one is an implementation of the last-saturation model and therefore only takes into account the properties of air parcels in the source and target regions. The second one additionally accounts for parameterized moisture sources and sinks during the advection of air parcels to the target region. Comparing the two types of reconstructions allows us to quantify the importance of changes in moisture sources and sinks in causing the relative humidity changes in our sensitivity experiments. To our knowledge, the last-saturation model has neither been used to understand differences between models, nor has it been implemented based on wind fields of simulations at storm-resolving resolution. This study therefore also represents a test of how useful the last-saturation model is in explaining differences between models as they begin to resolve the spectrum of vertical motions in the atmosphere.

This paper is organized as follows: Section 2 describes the model setup and the sensitivity experiments performed. In Section 3 the humidity changes produced in our sensitivity experiments are shown and discussed. The Lagrangian relative humidity reconstructions based on back-trajectories are introduced in Section 4. Section 5 presents insights on the mechanisms behind the humidity changes from the last-saturation model.

2 Model and experiments

To examine how changes in model parameterizations and model resolution affect tropical relative humidity in a GSRM, we run a series of sensitivity experiments with the ICOsahedral Nonhydrostatic model (ICON; Zängl et al., 2015) in its storm-resolving "Sapphire" configuration (Hohenegger et al., 2022) with prescribed sea surface temperature (SST).

2.1 Control experiment

The control experiment is run with a quasi-uniform horizontal grid spacing of 5 km. For the analysis, the model output is interpolated from the native icosahedral ICON grid to a regular $0.1^\circ \times 0.1^\circ$ latitude-longitude grid. The vertical grid consists of 110 hybrid sigma height levels between the surface and a height of 75 km. Over a flat surface at sea level, the distance between model levels in the free troposphere (between about 8 km to 19 km) is constant at 400m, gradually decreasing towards the surface and increasing towards the model top. The model time step is 40 seconds. For the treatment of microphysical processes, a one-moment scheme with five hydrometeor categories as described by Baldauf et al. (2011) is used. Turbulent mixing is represented by a classical 3D Smagorinksy scheme (Smagorinsky, 1963) with the modification by Lilly (1962) to account for thermal stratification (Dipankar et al., 2015). Radiative transfer is calculated at every grid point every 15 minutes using the RTE-RRTMGP scheme (Pincus et al., 2019). The JSBACH land model (Raddatz et al., 2007) is used to represent the physical properties of the land surface and land-atmosphere interactions.

The experimental protocol of our experiments closely follows that specified by the DYAMOND inter-model comparison (Stevens et al., 2019), with initial conditions taken from the global (9km) analysis by the European Centre of Medium Range Weather Forecast (ECMWF). After initialization, the simulations run freely without further forcing. ECMWF operational daily SST and sea-ice concentration are used as boundary conditions. The simulations start at 0 UTC on 27 June 2021 and span a time period of 45 days.

To test the extent to which humidity differences in our 45-day simulations might reflect sampling error, we perform a second control experiment (Control 2) with perturbed initial conditions. While the boundary conditions are kept identical to those in the control run, the atmosphere is initialised from the ECMWF analysis for 0 UTC on 28 June 2021, i.e. one day later than in the control experiment.

2.2 Sensitivity experiments

The changes we apply in our sensitivity experiments are chosen to resemble differences in model configuration across the DYAMOND models (Stevens et al., 2019), which reflect current differences in modeling approaches between modeling groups. The DYAMOND models differ in various aspects of their configuration. On the one hand, they differ in the design of their dynamical core. While (with the exception of two models) they agree on the equations they solve (fully-compressible Navier-Stokes equations), they differ in their numerical grids and the numerical methods they use to solve the equations. This not only influences their "effective" resolution, but also conditions the behavior of the parameterizations which act on the grid scale. On the other hand, the models differ in the parameterizations they use to represent the effects of subgrid-scale processes. For the sensitivity experiments we have to concentrate on a subset of these differences that can be tested with the ICON model. We attempt to cover the different types of uncertainties by examining the sensitivity of relative humidity to the model resolution as well as two different parameterizations. Our sensitivity experiments are described in the following and summarized in Table 1.

Even if at 5 km most of the energy in the spectrum of vertical motions is resolved, the updrafts of most deep convective systems remain poorly resolved or aliased to larger scales. To test the extent to which relative humidity is affected by changes in model resolution we perform three experiments. In the $\Delta x/2$ experiment the horizontal grid spacing is halved relative to the control experiment to 2.5 km. For the $2\Delta z$ and $\Delta z/2$ exper-

iments the number of vertical levels is decreased to 55 and increased to 190, respectively. This results in a doubling and halving of the vertical grid spacing in the free troposphere relative to the control experiment to 800 m and 200 m, respectively. Note that by GSRM standards (if not by GCM standards) a vertical grid spacing of 800 m is exceptionally coarse and was not employed in any of the DYAMOND models.

In three further experiments we test the sensitivity of relative humidity to changes in the parameterizations of turbulence and microphysics. These parameterizations contain a large number of tunable parameters and we do not attempt to systematically test the sensitivity to all of them. Instead we focus on contrasting models, which we see as a more extreme case than parameter sensitivities, although in one case we also explore a common parameter sensitivity.

Storm-resolving models typically use turbulence paramterizations that are not well adapted to global simulations at kilometer-scales. On the one hand, regional storm-resolving models have often used turbulence closures designed for LES simulations (like the Smagorinsky-Lilly scheme used in our control simulation), although the underlying assumption that the truncation scale lies within the inertial range of three-dimensional homogeneous and isotropic turbulence (Lilly, 1967) is not satisfied at storm-resolving scales (e.g. Bryan et al., 2003). On the other hand, many of the global DYAMOND models employed turbulence schemes that were inherited from their coarser-resolution predecessors. Similarly, the storm-resolving version of the ICON model was run with a total turbulent energy (TTE) scheme (Mauritsen et al., 2007) that was originally used at much coarser resolutions in the early stages of its development (Mauritsen et al., 2022). To examine the impact of different turbulence parameterizations on relative humidity, we exchange the Smagorinsky scheme used in the control simulation with this TTE scheme. The two schemes differ in several aspects. The Smagorinsky scheme calculates both vertical and horizontal mixing of momentum and scalar variables (although we find that horizontal mixing tendencies of specific humidity are negligible compared to vertical mixing tendencies at 5 km horizontal resolution, see also Section 4.4). The exchange coefficients are specified using a mixing length scale that depends on height and the model grid spacing, the 3D wind shear and static stability. The TTE scheme, on the other hand, only represents vertical mixing. The turbulent exchange coefficients are specified using a height-dependent mixing length scale and a velocity scale. The latter is determined from a prognostic equation for TTE that takes into account shear production, dissipation, third-order flux divergence and buoyancy production, which allows for mixing in more stably stratified situations than in the ICON implementation of the Smagorinsky-Lilly model.

To test the sensitivity of relative humidity to the microphysics parameterization, in the 2-mom experiment we exchange the one-moment scheme with the two-moment scheme by Seifert and Beheng (2001). While the DYAMOND models all use one-moment schemes, this mainly reflects the consensus that the scheme should be computationally efficient. The degree of complexity required in the cloud microphysics is an open question, and more complex two-moment schemes have also been proposed for storm-resolving simulations (e.g. Morrison et al., 2005; Phillips et al., 2007). The one-moment and two-moment microphysics implemented in ICON differ in many of their parameters, so changes emerging in the 2-mom experiment do not only result from the fact that two moments instead of one moment of the particle size distributions are predicted.

In an additional microphysics experiment, the $2v_{\mathrm{ice}}$ experiment, we perturb the one-moment microphysics by increasing the terminal fall speed of ice particles v_{ice}, which represents a common tuning parameter. In the one-moment scheme it is parameterized as

Table 1. Summary of simulations performed with the ICON model.

Name	Description
Control	Control simulation with 5 km horizontal grid spacing, 110 vertical levels (400 m grid spacing in the free troposphere), three-dimensional Smagorinsky turbulence and one-moment microphysics
Control 2	As Control, but with perturbed initial conditions to estimate internal variability
$\Delta x/2$	Horizontal grid spacing halved to 2.5 km
$2\Delta z$	Number of vertical levels reduced to 55 (800 m grid spacing in the free troposphere)
$\Delta z/2$	Number of vertical levels increased to 190 (200 m grid spacing in the free troposphere)
TTE	Turbulence scheme exchanged by a one-dimensional total turbulent energy (TTE) scheme
2-mom	Microphysics scheme exchanged by a two-moment scheme
$2v_{\mathrm{ice}}$	Increased (approximately doubled) fall speed of ice particles in the one-moment microphysics

a function of ice mass mixing ratio q_{ice} and air density ρ:

$$v_{\mathrm{ice}} = a(\rho q_{\mathrm{ice}})^b(\rho_0/\rho)^c \tag{1}$$

with $\rho_0 = 1.225\,\mathrm{kg\,m^{-2}}$ is the air density at surface conditions. The parameters a, b and c are set to 1.25, 0.16 and 0.33, respectively. For our sensitivity experiment we increase a to 3.29, which corresponds to the value originally proposed by Heymsfield and Donner (1990), and c to 0.4, thereby moving it closer to the value of 0.5 used in the two-moment scheme of ICON. Combined, these changes approximately double the fall speed of ice particles for a given q_i and ρ.

3 Sensitivity of relative humidity to changes in model resolution and parameterizations

Figure 1 shows how the tropical mean vertical profile of relative humidity changes in our sensitivity experiments. Here, relative humidity $\mathcal{R}$ is calculated as

$$\mathcal{R} = \frac{q}{q^*(T,p)} \tag{2}$$

with the specific humidity q and the saturation specific humidity $q^* = \frac{\frac{M_w}{M_d}e^*(T)}{p-(1-\frac{M_w}{M_d})e^*(T)}$, where e^* is the saturation water vapor pressure at temperature T, p is the pressure and M_w and M_d are the molar masses of water vapor and dry air, respectively. For e^* we take the value with respect to water for T above the triple point of water T_t and the value with respect to ice for T below $T_t - 23\,\mathrm{K}$. For intermediate T a combination of both is used following the documentation of the Integrated Forecast System (ECMWF, 2018). Note that a more common definition of relative humidity uses saturation water vapor pressure instead of specific humidity. We use equation 2 to make the definition of $\mathcal{R}$ consistent with the one we use for the Lagrangian reconstructions in Section 4. This definition is typically used in last-saturation studies (e.g. Sherwood et al., 2010) since specific humidity is the conserved quantity after last-saturation. Numerically, the difference between the two definitions is typically within 1%.

First it is worth noting that the $\mathcal{R}$ spread produced by our experiments is similar to the inter-model spread in the DYAMOND ensemble (Figure 1c). Based on the DYAMOND ensemble, Lang et al. (2021) showed that the $\mathcal{R}$ spread across GSRMs is reduced compared to classical GCMs. This is possibly related to the omission of convective parameterisations, which represent a major source of uncertainty in GCMs. Our experiments support this by showing that even strong perturbations in GSRMs do not reproduce the spread across models with convective parameterizations.

Of the experiments with changed model resolution the largest changes in $\mathcal{R}$ are seen in the $2\Delta z$ experiment with reduced vertical resolution (Figure 1a,b). $\mathcal{R}$ increases particularly in the upper troposphere, where the difference to the control experiment exceeds 10%. In line with this, increasing the vertical resolution ($\Delta z/2$) reduces $\mathcal{R}$ in the upper troposphere. However, the magnitude of the drying is much smaller than the moistening in the $2\Delta z$ experiment, so the $\mathcal{R}$ profile shows signs of convergence at vertical resolutions around the one used in the control experiment. Increasing the horizontal resolution ($\Delta x/2$) also only leads to a minor increase of $\mathcal{R}$ in the lower and mid troposphere. Given that the $2\Delta z$ experiment represents a rather extreme case, in the sense that GSRMs are not commonly run at such coarse vertical resolution, these results suggest that changing model resolution within the general scale of GSRM resolution does not represent a major uncertainty for $\mathcal{R}$, unless it is chosen exceptionally coarse. Note that this does not exclude the possibility that increasing resolution to even finer scales (on the order of 200 m) could make a significant difference, which cannot be tested with the chosen setup and available computational resources.

Comparably large $\mathcal{R}$ changes occur in the TTE and 2-mom experiments, in which the parameterizations of turbulence and microphysics were changed. The largest changes occur in the lower and mid troposphere, where they have a larger impact on the clear-sky OLR than those in the upper troposphere (Lang et al., 2021). Changing to the TTE turbulence scheme results in a strong increase in $\mathcal{R}$ of up to 8% over a broad altitude layer between 2 km to 6 km. This change will be examined in more detail in the following sections as part of our last-saturation analysis of the mid troposphere. Changing to the 2-mom microphysics scheme leads to a strong (up to 10%) decrease in $\mathcal{R}$ that is concentrated in a rather shallow layer between 1 km and 3 km in the lower free troposphere. Dividing the tropics into different moisture regimes also shows that this drying is concentrated in the dry subsidence regimes of the tropics, where shallow clouds prevail (not shown). This might indicate that the details in the formulation of the microphysics matter particularly in the shallow cloud regime, where humidity is not as strongly constrained by the dynamics as in deep convective regimes. Increasing the fall speed of ice particles in the 1-mom scheme ($2v_{\mathrm{ice}}$) has a smaller effect on $\mathcal{R}$ than changing to the two-moment scheme. $\mathcal{R}$ slightly decreases in the mid to upper troposphere, whereas lower-tropospheric $\mathcal{R}$ is hardly affected. This may be expected, since ice particles mainly exist at higher altitudes with temperatures below the melting point (located at a height of about 5 km in our experiments). Changing between one- and two-moment microphysics, on the other hand, potentially affects the characteristics of all types of hydrometeors.

$\mathcal{R}$ changes in most sensitivity experiments are larger than the difference between the two control experiments (Control and Control 2) which serves as an estimate of internal variability. Exceptions are the very subtle changes in the $2v_{\mathrm{ice}}$ and $\Delta z/2$ experiments in the lower free troposphere and in the $\Delta x/2$ experiment in the upper troposphere. We conclude that the differences we find in tropical mean $\mathcal{R}$ mostly represent systematic differences resulting from the applied perturbations rather than internal variability.

Temperature profiles differ substantially between the experiments (Figure 1d). Temperature differences that exist in the lower troposphere intensify with increasing height, as is to be expected from temperature profiles following moist adiabats to first order. Warmest and coldest temperatures are produced by the TTE and $2v_{\mathrm{ice}}$ experiments, respectively. The 2-mom experiment stands out due to a positive temperature anomaly that is limited to the region between 1 km to 3 km, where the largest negative $\mathcal{R}$ anomaly is found. This points to a shallower trade inversion in the 2-mom experiment. This could be indicative of an earlier onset of precipitation in the 2-mom experiment, resulting in clouds growing less deep (Stevens & Seifert, 2008).

Based on a simple analytical model Romps (2014) showed that in radiative-convective equilibrium $\mathcal{R}$ should be an invariant function of temperature as the atmosphere warms. An obvious question is therefore if the changes in our sensitivity experiments are explained by an upward or downward shift of the $\mathcal{R}$ profile following an increase or decrease in temperature, respectively. This would mean that in experiments with a warmer troposphere $\mathcal{R}$ should increase in the lower and mid troposphere, where $\mathcal{R}$ decreases with height, and $\mathcal{R}$ should decrease in the upper troposphere, where $\mathcal{R}$ increases with height. While the TTE and 2-mom runs show a corresponding pattern in their $\mathcal{R}$ changes, the temperature differences between the experiments is by far not large enough to explain the $\mathcal{R}$ differences. This is evident when $\mathcal{R}$ is plotted as a function of temperature (not shown). We therefore conclude that the differences in $\mathcal{R}$ are not explained by a vertical shift following isotherms.

In summary, our experiments suggest that a large part of the $\mathcal{R}$ spread across today's GSRMs is can be explained by different formulations of small-scale mixing and cloud microphysical processes. At least in the limited number of experiments we performed, microphysical choices particularly impact $\mathcal{R}$ in a rather narrow altitude region associated with shallow convection, whereas the choice of the turbulence scheme affects $\mathcal{R}$ in a broader mid-tropospheric layer.

In the following we focus on $\mathcal{R}$ differences in the mid troposphere (4 km to 8 km, indicated by the gray lines in Figure 1). Although mid-tropospheric $\mathcal{R}$ differences are, similar as in the DYAMOND ensemble, not particularly large, Lang et al. (2021) showed that $\mathcal{R}$ differences in this region are particularly important for differences in OLR.

4 Lagrangian reconstructions of relative humidity

4.1 Reconstructions based on the last-saturation model

To obtain a better understanding of the physical mechanisms behind the humidity changes produced in our experiments we use a last-saturation framework based on back-trajectories. For this analysis we focus on the altitude region between 4 km and 8 km, where $\mathcal{R}$ differences in the DYAMOND ensemble were shown to have a comparably large effect on the clear-sky radiation budget (Lang et al., 2021). A main goal is to understand to what extent the changes in $\mathcal{R}$ are explained by changes in the properties of the source regions of air parcels, i.e. the points of last-saturation/condensation, and by changes in moisture sources and sinks during subsequent advection.

To investigate this we perform Lagrangian reconstructions of $\mathcal{R}$ for the ICON experiments described in Section 2. The reconstruction for each experiment is performed in two different ways. The first one is an implementation of the last-saturation paradigm similar to earlier studies (e.g. Sherwood, 1996; Dessler & Sherwood, 2000; Pierrehum-

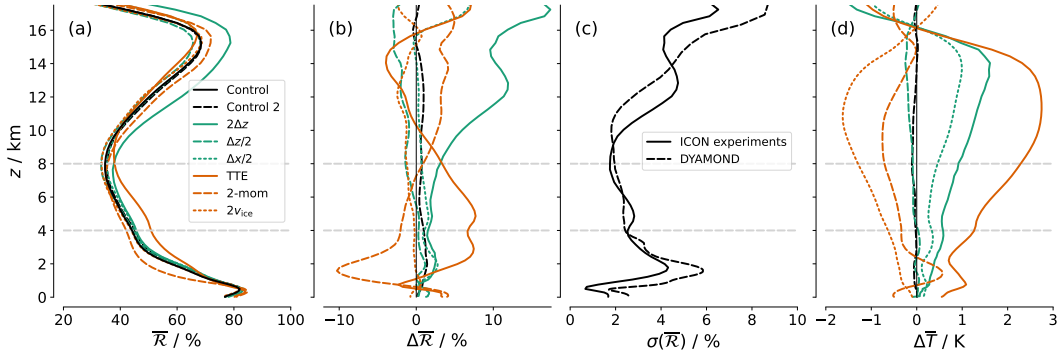

Figure 1. Changes in tropical mean relative humidity ($\overline{\mathcal{R}}$) and temperature ($\overline{T}$) resulting from changes in model resolution and parameterizations in the sensitivity experiments. (a) Vertical profiles of $\overline{\mathcal{R}}$ in control and sensitivity experiments, (b) change in $\overline{\mathcal{R}}$ compared to the control experiment and (c) standard deviation of $\overline{\mathcal{R}}$ across ICON experiments (solid) and the DYAMOND multi-model ensemble (dashed). (d) Change in temperature $\overline{T}$ compared to the control experiment. Horizontal dashed lines mark the altitude region between 4 km and 8 km, for which the mechanisms behind the $\mathcal{R}$ changes are investigated based on back-trajectories.

bert & Roca, 1998), although the latter were based on much coarser wind fields from GCMs or reanalysis data. The underlying assumption is that specific humidity q is conserved after the last-condensation event. Hence, the specific humidity at a given target point q_t equals the specific humidity the respective parcel had when it last experienced condensation q_lc. $\mathcal{R}$ at the target point is then equal to

$$\mathcal{R}_\mathrm{lc} = \frac{q_\mathrm{lc}}{q_\mathrm{t}^*}, \tag{3}$$

where q_t^* denotes the saturation specific humidity at the target point. q_lc should generally equal its saturation value q_ls^* (though supersaturation can occur with respect to ice), so that Equation 3 can be written as

$$\mathcal{R}_\mathrm{lc} \approx \frac{q_\mathrm{ls}^*}{q_\mathrm{t}^*} = \frac{e^*(T_\mathrm{lc})}{e^*(T_\mathrm{t})}\frac{p_\mathrm{t}}{p_\mathrm{lc}}, \tag{4}$$

where e^* is the saturation water vapour pressure, T_lc and T_t are the temperatures of the last-condensation point and the target point, respectively, and p_lc and p_t are the corresponding air pressures. Thus, if the last-saturation reconstruction captures the humidity changes in the ICON experiments, this means that they are explained by temperature and pressure changes between the source and target regions.

For the reconstructions we use the actual q_lc rather than q_ls^*, i.e. Equation 3 rather than Equation 4, since $\mathcal{R}$ is not always exactly 100% at the instant of last-condensation (see Section 4.3). This slightly improves our reconstructions, but our main conclusions do not depend on whether or not $q_\mathrm{lc} = q_\mathrm{ls}^*$ is assumed for the last-saturation events. The terms last-condensation and last-saturation are used interchangeably in the following.

For the second reconstruction of $\mathcal{R}$ moisture sources and sinks s, which can change a parcel's water vapour content during its advection after the last-condensation event, are added:

$$\mathcal{R}_\mathrm{lc+s} = \frac{q_\mathrm{lc} + s}{q_\mathrm{t}^*}. \tag{5}$$

s includes evaporation of hydrometeors that are transported with or sediment through an air parcel, as well as turbulent mixing. These processes are represented by the parameterizations of microphysics and turbulence in the ICON model. As we will show in Section 4.6, the inclusion of these sources and sinks brings the reconstructed $\mathcal{R}$ closer to the ICON-simulated $\mathcal{R}$ (subsequently denoted by $\mathcal{R}_{\mathrm{ICON}}$).

Using the reconstructions, the change in $\mathcal{R}$ between a sensitivity experiment and the control experiment can be decomposed into three contributions:

$$\Delta\mathcal{R}_{\mathrm{ICON}} = \Delta\mathcal{R}_{\mathrm{lc}} + \Delta(\mathcal{R}_{\mathrm{lc+s}} - \mathcal{R}_{\mathrm{lc}}) + \Delta r. \tag{6}$$

The first term on the right hand side represents changes in source and/or target region pressure and temperature. The second term denotes the effect of changes in parameterized moisture sources and sinks acting during advection to the target region. The residual r is the difference $\mathcal{R}_{\mathrm{ICON}} - \mathcal{R}_{\mathrm{lc+s}}$. It results from shortcomings in the reconstruction method (Sections 4.2 to 4.6), but also from the fact that the Lagrangian reconstruction does not include any numerical diffusion, as opposed to the Eulerian advection scheme in ICON. Hence, the Δr term includes changes in numerical diffusion, which might be important in the experiments with changed model resolution but is not captured by the Lagrangian reconstruction.

The methods used to determine the points of last-condensation and the moisture sources and sinks along back-trajectories are described in the following.

4.2 Back-trajectories

Back-trajectories are calculated offline using the ICON version of the trajectory tool LAGRANTO version 2.0 (Wernli & Davies, 1997; Sprenger & Wernli, 2015). An ensemble of 150,000 back-trajectories is released once per day at 12 UTC from randomly selected points in the tropics (30°S to 30°N) between 4 km and 8 km height. In the following we will refer to this region as the target region.

Comparing the $\mathcal{R}$ distribution of the 150,000 trajectory starting points to the one obtained from the full field showed that the sampling error is small compared to the $\mathcal{R}$ differences between the model experiments. By starting the trajectories at 12 UTC only, depending on longitude we sample at different local times and thus capture different phases of the diurnal cycle of free-tropospheric humidity. A comparison showed that when sampling at 0 UTC, the moistest tropical regions appear moister by about 2% than when sampling at 12 UTC. This is likely a signature of the diurnal cycle of global precipitation, which was highlighted by Stevens et al. (2019). The effect of the sampling on the humidity differences between two experiments is small because the effect of the diurnal cycle is similar in each experiment. As our main interest is in the differences between experiments we conclude that starting trajectories once per day is sufficient.

Trajectories are integrated backwards in time for 15 days based on 1-hourly instantaneous 3D model wind fields. Out of a total of 45 simulated days, due to the 15-day lead time for the back-trajectories and the omission of the first five simulated days due to model spinup, a 25-day period remains for the Lagrangian reconstructions.

Given that the trajectory calculations are based on hourly model wind fields, and that the transport algorithms we use neither share the same numerical methods used by the ICON model nor are performed on the same grid, individual trajectories are not accurate, in the sense that they do not necessarily follow the exact paths they would fol-

low if they were calculated online during model integration (Miltenberger et al., 2013). However, from a large ensemble of back-trajectories it is possible to infer the statistical properties of the points of last condensation and subsequent moisture sources and sinks, as we will show in the following.

4.3 Last-condensation events

We define the point of last condensation to be the first point along a back-trajectory, for which the local moisture tendency from the microphysics parameterization $(\frac{\mathrm{d}q}{\mathrm{d}t})_{\mathrm{mic}}$ takes on a negative value, i.e. as the point at which condensation last occurred. We decided for this definition rather than using a threshold value on relative humidity, because the critical relative humidity for condensation in ICON can exceed 100% with respect to ice. As a result of the spatial interpolation of the model fields, both the interpolation from the native ICON grid to a latitude-longitude grid and the interpolation from the latitude-longitude grid onto the trajectory positions performed by LAGRANTO, there are points where $(\frac{\mathrm{d}q}{\mathrm{d}t})_{\mathrm{mic}} < 0$ (and are therefore detected as condensation points), but the local relative humidity is significantly smaller than 100%. We therefore introduce the additional condition that the local relative humidity must be higher than 80%. If this condition is not met, the search for a last-condensation event is continued backwards along the trajectory.

Last-condensation events identified by this method are subject to different uncertainties. Condensation events will be missed if they occur in between the 1-hourly model output time step, which our trajectories are calculated on. We expect this to introduce a dry bias in the reconstructed $\mathcal{R}$, since on average the identified last-condensation events occur too far in the past and therefore at too cold temperatures, assuming that most air parcels undergo subsidence on their way to the target region. Furthermore, the last-condensation events we determine are restricted to the 15-day period covered by the back-trajectories, so events occurring further in the past are not detected. We do not find a last-condensation event within 15 days for 7% of the trajectories. This is expected to introduce a moist bias in the reconstructed $\mathcal{R}$, assuming that the condensation events further back in time would occur at higher altitudes and therefore colder temperatures than the trajectory end points.

4.4 Moisture sources and sinks from parameterized processes

To estimate the magnitude of moisture sources and sinks S (Equation 5), along each trajectory we sum up the local tendencies of q from the microphysics and turbulence parameterizations $(\frac{\mathrm{d}q}{\mathrm{d}t})_{\mathrm{mic}}$ and $(\frac{\mathrm{d}q}{\mathrm{d}t})_{\mathrm{turb}}$, respectively, between the time of last condensation t_{lc} and the target point ($t = 0$):

$$s = \sum_{t=0}^{t_{\mathrm{lc}}} ((\frac{\mathrm{d}q}{\mathrm{d}t})_{\mathrm{mic,t}} + (\frac{\mathrm{d}q}{\mathrm{d}t})_{\mathrm{turb,t}})\Delta t, \tag{7}$$

where $\Delta t = 1\,\mathrm{h}$ is the model output interval. The moisture tendency from the turbulence scheme $(\frac{\mathrm{d}q}{\mathrm{d}t})_{\mathrm{turb}}$ output by ICON only includes the contribution from vertical mixing, although the Smagorinsky turbulence scheme also performs horizontal mixing. Including the contribution from horizontal mixing for one of the ICON experiments showed it to be negligible compared to the effect of vertical mixing.

4.5 Spatial averaging

Figures 2a and 2b show the (randomly chosen) start positions of back-trajectories for an exemplary simulation time step on a map. Each dot corresponds to one start position, colored by the ICON-simulated relative humidity ($\mathcal{R}_{\mathrm{ICON}}$) and reconstructed relative humidity ($\mathcal{R}_{\mathrm{lc+s}}$), respectively, for the respective position. Target regions for which $\mathcal{R}_{\mathrm{ICON}}$ takes on intermediate values show up as a mixture of very high and very low values in $\mathcal{R}_{\mathrm{lc+s}}$. This is likely due to the fact that gradients and extremes in $\mathcal{R}_{\mathrm{ICON}}$ are smoothed out due to the limited resolution of the ICON model. While each value of $\mathcal{R}_{\mathrm{ICON}}$ in Figure 2a represents a grid-cell average, values of $\mathcal{R}_{\mathrm{lc+s}}$ in Figure 2b represent structures (or "filaments") on smaller scales, which are not resolved on the ICON grid. To smooth the reconstructed fields the sampling would need to be improved by increasing the number of trajectories per ICON grid cell and averaging over them. Another source of noise in the reconstructed $\mathcal{R}$ are inaccuracies in the trajectories, which result from the coarse (1-hourly) temporal resolution and spatial interpolation of the input data (see Section 4.2). These inaccuracies can result in last-condensation points being spatially displaced from their true position.

To minimize sampling biases and to make our analysis framework more commensurate with the information content in the input data we coarsen our analysis region by averaging all results within boxes that span an area of $2^\circ \times 2^\circ$ in the horizontal and the complete altitude range between 4 km and 8 km in the vertical. These boxes will be referred to as target boxes in the following. We predict the horizontally and vertically averaged relative humidity in each target box as the mean of $\mathcal{R}_{\mathrm{lc}}$, respectively $\mathcal{R}_{\mathrm{lc+s}}$, of all back-trajectories released from within the box. As shown in Figure 2c and 2d, there is good agreement between the spatially averaged $\mathcal{R}_{\mathrm{ICON}}$ and $\mathcal{R}_{\mathrm{lc+s}}$, though the reconstructed field is still a bit noisier.

For some trajectories, the Lagrangian reconstruction yields extreme, unphysically high values of $\mathcal{R}$. In these cases the last-condensation event occurred at higher temperatures than that of the target point, so the air parcels have ascended after the last-condensation event. The ascent and associated cooling would not be possible without further condensation, which would keep the air parcel's relative humidity at around 100%. However, due to the shortcomings in our method described in Sections 4.2 and 4.3, these further condensation events are missed and an extremely high value of $\mathcal{R}$ is predicted. We remove these cases prior to the spatial averaging by discarding trajectories for which $\mathcal{R}_{\mathrm{lc+s}}$ is more than 10% higher than the maximum of $\mathcal{R}_{\mathrm{ICON}}$, which is about 130% in the control experiment. This is the case for 5% of all trajectories for which a last-condensation event was determined.

4.6 Reconstructed relative humidity

To evaluate the methods described above, we examine how well $\mathcal{R}_{\mathrm{ICON}}$ is reproduced by Equations 3 and 5 in our control experiment. The distribution of $\mathcal{R}_{\mathrm{ICON}}$ is bimodal with a prominent peak at values below 20% (Figure 3). Such a bimodal distribution is well known from observations (e.g. Zhang et al., 2003; Ryoo et al., 2009) and has been attributed to the rapid drying by radiative subsidence; after being moistened by upward transport, air parcels dry out rapidly and spend a short time at intermediate humidity (Mapes, 2001).

Both kinds of Lagrangian reconstructions reproduce the ICON-simulated $\mathcal{R}_{\mathrm{ICON}}$ well (Figure 3). While the distribution of $\mathcal{R}_{\mathrm{lc}}$ is shifted to lower values compared to $\mathcal{R}_{\mathrm{ICON}}$, the distribution of $\mathcal{R}_{\mathrm{lc+s}}$ is closer to, but shifted to slightly higher values than $\mathcal{R}_{\mathrm{ICON}}$.

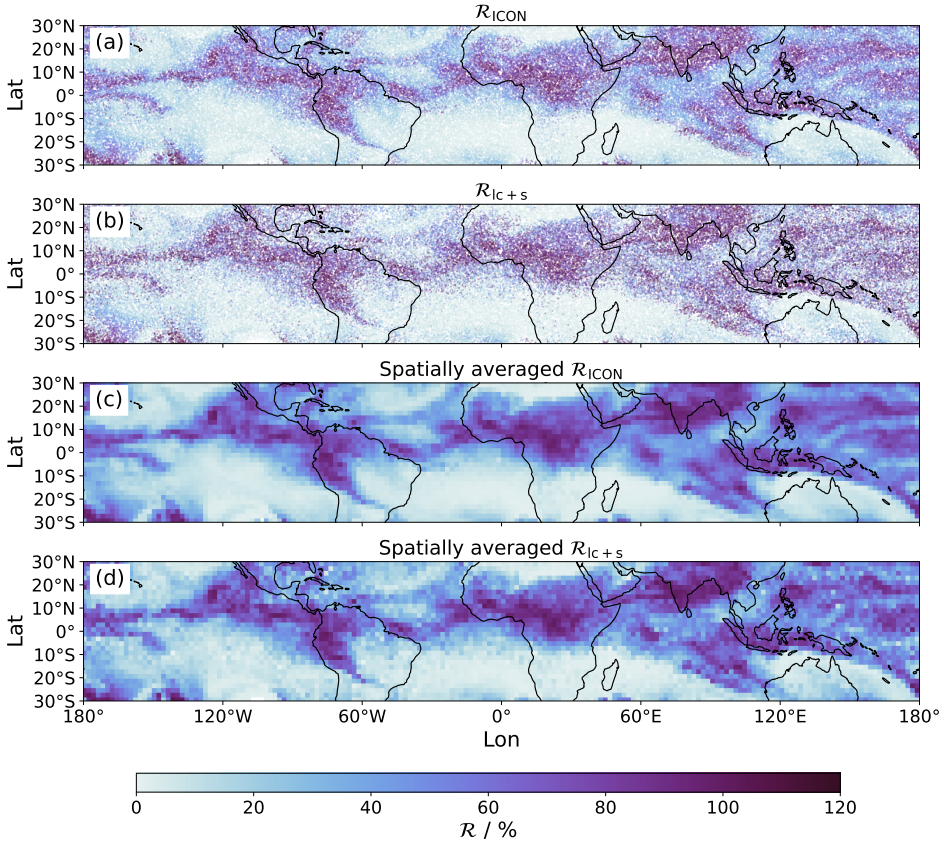

Figure 2. Illustration of spatial averaging performed to reduce noise in the reconstructed relative humidity field for an exemplary time step (17 July 2021, 12Z). Scatterplots of (a) ICON-simulated relative humidity ($\mathcal{R}_{\mathrm{ICON}}$) and (b) reconstructed relative humidity $\mathcal{R}_{\mathrm{lc+s}}$ at the start positions of back-trajectories. Spatially averaged (c) $\mathcal{R}_{\mathrm{ICON}}$ and (d) $\mathcal{R}_{\mathrm{lc+s}}$ over $2^\circ \times 2^\circ$ boxes.

The improvement of the reconstruction by including moisture sources and sinks is encouraging, as this would be expected if the approach was working as intended. The fact that the inclusion of moisture sources and sinks from the parameterizations increases the predicted relative humidity is not surprising. Per definition, microphysical processes can only increase an air parcel's q after the point of last condensation. Turbulent mixing can generally either increase or decrease q. However, vertical mixing, which dominates along our trajectories (see Section 4.4), primarily moistens air parcels that subside through the free troposphere due to a down gradient moisture flux and the exponential decrease of q with height. Why $\mathcal{R}_{\mathrm{lc+s}}$ tends to overestimate $\mathcal{R}_{\mathrm{ICON}}$ is less clear and likely reflects uncertainties in our method and/or the fact that the Lagrangian reconstruction does not incorporate numerical diffusion. However, the aim of the Lagrangian reconstruction in this study is not to obtain a perfect reproduction of $\mathcal{R}_{\mathrm{ICON}}$, but rather to explain humidity differences between different ICON experiments. As we will show in Section 5.2, this is possible despite some small deviations of the $\mathcal{R}_{\mathrm{lc+s}}$ distribution to the $\mathcal{R}_{\mathrm{ICON}}$ distribution.

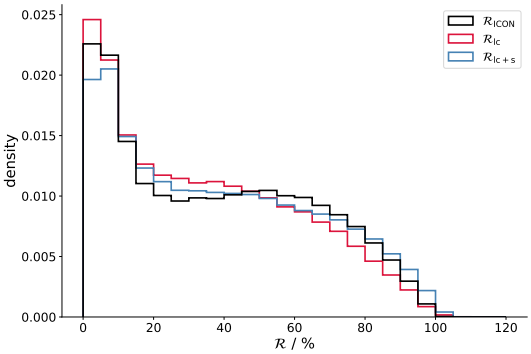

Figure 3. ICON-simulated and reconstructed relative humidity distributions in the control experiment. Probability density of tropical relative humidity simulated by the ICON model ($\mathcal{R}_{\mathrm{ICON}}$, black) as well as from Lagrangian reconstructions based on the plain last-saturation model ($\mathcal{R}_{\mathrm{lc}}$, red) and taking into account moisture sources and sinks from parameterized processes ($\mathcal{R}_{\mathrm{lc+s}}$, blue). Histograms are based on $2^\circ \times 2^\circ$ spatially averaged relative humidity (see text for details).

4.7 $\mathcal{R}$-space

To distinguish between different tropical humidity regimes, we divide the target boxes and the corresponding back-trajectories into ten equal-sized bins of $\mathcal{R}_{\mathrm{ICON}}$. The driest bins in this "$\mathcal{R}$-space" correspond to the (sub-)tropical subsidence regions, whereas the moistest bins correspond to deep convective regions in the Intertropical Convergence Zone (ITCZ) and the Indo-Pacific Warm Pool. In our experiments, which are performed for a period in northern-hemisphere summer, the regions of highest $\mathcal{R}$ are centered around about 10° N and the driest regions are concentrated south of the equator, where the subsiding branch of the strong cross-equatorial Hadley cell is located (Figure 4a). Regions of intermediate $\mathcal{R}$ are more widely distributed across the tropics, with a larger proportion located north of the equator.

The back-trajectories demonstrate how the origins of air parcels differ between regions of low and high $\mathcal{R}$. For the driest target regions south of the equator, last condensation occurs in two different regions remote from the target region: on the southern edge of the tropical deep convective regimes close to the equator, and in the sub- and extratropics (Figure 4b). Towards regions of higher $\mathcal{R}$, the fraction of air parcels originating from within the tropics increases (Figure 4c). Air parcels arriving in the driest regimes have on average travelled for about one week since last condensation (Figure 4c), which is consistent with the time periods found by Cau et al. (2007) based on reanalysis fields. These air parcels have subsided from high altitudes, as evident from low last-condensation temperatures of about 220 K. The large difference between source and target temperature causes the extremely low target $\mathcal{R}$ of these parcels (Equation 4). In summary, regions of low $\mathcal{R}$ are characterized by source regions that are cold and remote. Towards regions of higher $\mathcal{R}$, last-condensation events occur closer to the target regions and at temperatures more similar to that of the target region (Figure 4b,c). Air parcels arriving in the moistest target regions have travelled for less than a day since last condensation.

Figure 5a shows mean and standard deviation of the reconstructed $\mathcal{R}_{\mathrm{lc}}$ and $\mathcal{R}_{\mathrm{lc+s}}$, respectively, plotted against mean $\mathcal{R}_{\mathrm{ICON}}$ for each bin in $\mathcal{R}$-space for the control exper-

iment. The spread in the reconstructed $\mathcal{R}$ in each bin is comparable to the difference in $\mathcal{R}_{\mathrm{ICON}}$ between neighbouring bins, demonstrating that the Lagrangian reconstruction succeeds in predicting the $\mathcal{R}$ of a given target box. Again, it is evident that the plain last-saturation reconstruction underestimates $\mathcal{R}$, particularly in moist regimes, while the reconstruction with moisture sources and sinks slightly overestimates $\mathcal{R}$, particularly in dry regimes.

The difference between $\mathcal{R}_{\mathrm{lc+s}}$ and $\mathcal{R}_{\mathrm{lc}}$ provides an estimate of the effect of parameterized moisture sources on relative humidity. It increases from about 0.5% in the driest decile to about 6% in the moistest decile (Figure 5b). Although parcels that end up with low $\mathcal{R}$ also originate from moist regions, where microphysical processes and turbulent mixing are potentially active, they passed these regions at much colder temperatures (cf. Figure 4c), at which water vapor concentrations (and hence also sources) are small. Therefore, the effect from parameterized moisture sources on $\mathcal{R}$ increases from dry to moist regions when it is measured in absolute units. When the change in $\mathcal{R}$ from parameterized sources is measured relative to the final (reconstructed) value of $\mathcal{R}$ it decreases from about 15% in the driest decile to about 5% in the moistest decile. This reflects that the probability to encounter moisture sources is enhanced for parcels that end up with low $\mathcal{R}$, because they have been transported over a longer time since last condensation (cf. Figure 4c). In general, the difference between $\mathcal{R}_{\mathrm{lc+s}}$ and $\mathcal{R}_{\mathrm{lc}}$ is small compared to the range of $\mathcal{R}$ values occurring throughout the tropics. This is in line with many earlier studies, which concluded that moisture sources and sinks are not relevant for explaining spatial variations of tropical $\mathcal{R}$ (e.g. Sherwood, 1996; Dessler & Sherwood, 2000), corroborating the general validity of the last-saturation paradigm. Nevertheless, they might be relevant for explaining more subtle $\mathcal{R}$ differences between model experiments. This will be examined in the course of this study.

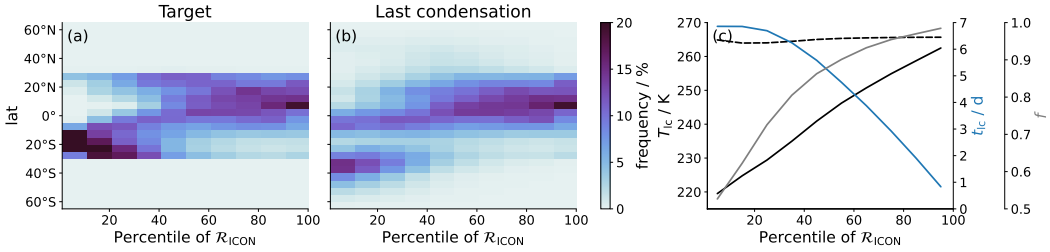

Figure 4. Characteristics of target and source regions in the control experiment in $\mathcal{R}$-space. Histograms showing meridional distributions of (a) target regions and (b) last-condensation points for ten decile-bins of $\mathcal{R}_{\mathrm{ICON}}$. (c) Bin-averages of last-condensation temperature (T_{lc}, black solid) and time passed since last condensation (t_{lc}, blue), as well as fraction of last-condensation points located within the tropics, defined as 30° S to 30° N (f, gray). The temperature of the target region is denoted by the black dashed line.

5 Mechanisms controlling mid-tropospheric relative humidity differences

5.1 Changes in mid-tropospheric relative humidity

The representation of mid-tropospheric $\mathcal{R}$ differences in $\mathcal{R}$-space (Figure 6a) shows that for most experiments changes in $\mathcal{R}$ are larger in moist than in dry regions. Therefore, differences in tropical mean $\mathcal{R}$ (Figure 1) mainly reflect differences in the moist re-

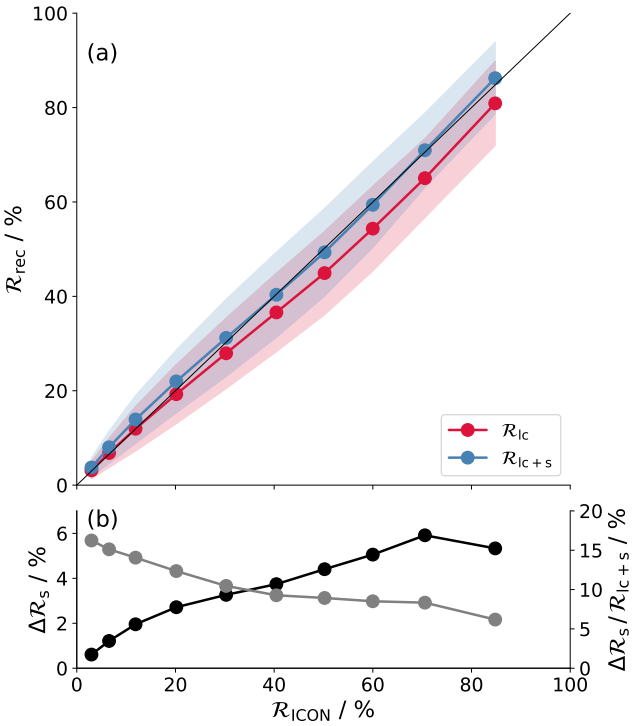

Figure 5. ICON-simulated and reconstructed relative humidity $\mathcal{R}$ for the control experiment in $\mathcal{R}$-space. (a) Reconstructed $\mathcal{R}$ ($\mathcal{R}_{rec}$) versus ICON-simulated $\mathcal{R}$ ($\mathcal{R}_{ICON}$) for ten decile-bins of $\mathcal{R}_{ICON}$. Points correspond to bin-mean values, the shading indicates ± one standard deviation of $\mathcal{R}_{rec}$. Colours distinguish reconstructions based on the plain last-saturation model ($\mathcal{R}_{lc}$, red) and taking into account moisture sources and sinks from parameterized processes ($\mathcal{R}_{lc+s}$, blue). (b) The difference $\mathcal{R}_{lc+s} - \mathcal{R}_{lc}$ ($\Delta\mathcal{R}_s$) in absolute units (black, left x-axis) and relative to $\mathcal{R}_{lc+s}$ (gray, right x-axis).

gions. A similar behaviour was also found for mid-tropospheric humidity differences among the DYAMOND models (Lang et al., 2021). The robustness of $\mathcal{R}$ in dry regions is related to their cold source temperatures, which will be discussed in more detail in Section 5.3.

As already evident from the tropical mean $\mathcal{R}$ profiles, mid-trospheric $\mathcal{R}$ changes are largest in the experiment with the TTE turbulence scheme. The representation in $\mathcal{R}$-space shows that $\mathcal{R}$ increases throughout the tropics, but the strongest increase (about 10%) occurs in rather moist regimes around the 80th percentile of $\mathcal{R}$. In comparison, the sensitivity of mid-tropospheric $\mathcal{R}$ to changes in the microphysics (2-mom and $2v_{ice}$) is weaker and limited to regions of intermediate and high $\mathcal{R}$. The experiment with halved vertical resolution ($2\Delta z$) is the only one in which changes in $\mathcal{R}$ are larger in dry than in moist regimes. The increase in mid-tropospheric $\mathcal{R}$ in the experiment with doubled horizontal resolution ($\Delta x/2$) is concentrated in moist regimes.

Internal variability, which we estimate from the difference between the two control experiments, is larger in dry than in moist regions. This may be expected given that the source regions of dry air are remote (Figure 4) and therefore strongly influenced by the large-scale circulation, which varies on timescales that are longer than our simulation

period. While in the moist regions (and therefore also in the tropical mean) changes in $\mathcal{R}$ are larger than the estimated internal variability in all sensitivity experiments, in the dry regions this is only the case for the TTE and $2\Delta z$ experiments. Thus, the $\mathcal{R}$ differences we find in dry regions are strongly coloured by internal variability and systematic differences could only be quantified based on longer experiments. This should be kept in mind for the discussions in the following.

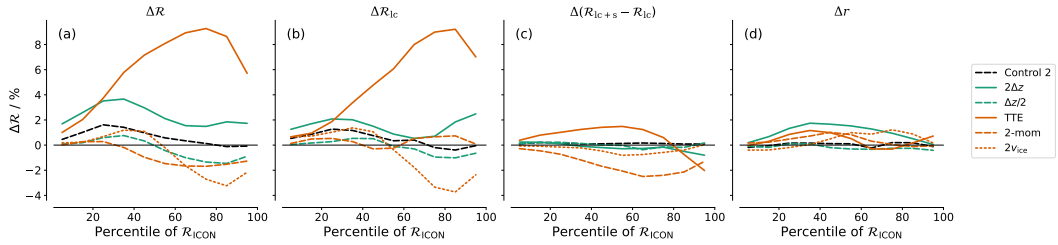

Figure 6. ICON-simulated and reconstructed changes in mid-tropospheric $\mathcal{R}$ in the sensitivity experiments displayed in $\mathcal{R}$-space. (a) Changes in ICON-simulated $\mathcal{R}$ compared to the control experiment ($\Delta\mathcal{R}_{\mathrm{ICON}}$). (b) Changes in $\mathcal{R}$ reconstructed by a plain last-saturation model ($\Delta\mathcal{R}_{\mathrm{lc}}$) and (c) changes in the effect of moisture sources and sinks after last condensation ($\Delta(\mathcal{R}_{\mathrm{lc+s}}-\mathcal{R}_{\mathrm{lc}})$). (d) Changes in the residual (Δr), i.e. in the difference between ICON-simulated and reconstructed $\mathcal{R}$. The sum of the terms shown in (b) to (d) yields the ICON-simulated $\mathcal{R}$ changes shown in (a). Lagrangian reconstructions were not performed for the $\Delta x/2$ experiment (see text for explanation).

5.2 Changes in source and target regions vs. changes during advection

The two types of Lagrangian reconstructions (Equations 3 and 5) are used to shed light on the physical processes behind the $\mathcal{R}$ changes in the sensitivity experiments. The reconstructions were performed for all experiments except the $\Delta x/2$ experiment for reasons of limited resources as the doubled horizontal resolution increases the model output by a factor of four. Additionally, to obtain the same accuracy of trajectories as for the control experiment the timestep for the trajectory calculation would need to be halved. In total, the required model output for the $\Delta x/2$ experiment would increase by a factor of 8 and the trajectory calculations would get correspondingly expensive.

For most experiments the $\mathcal{R}$ differences that were reconstructed based on the plain last-saturation model ($\Delta\mathcal{R}_{\mathrm{lc}}$, Figure 6b) explain a large part of the actual differences ($\Delta\mathcal{R}_{\mathrm{ICON}}$, Figure 6a), whereas the effect from changes in parameterized processes given by $\Delta\mathcal{R}_{\mathrm{lc+s}}-\Delta\mathcal{R}_{\mathrm{lc}}$ is small (Figure 6c). This means that the $\mathcal{R}$ changes must be mainly caused by changes in the source and/or target temperature (see also Section 5.3), whereas changes in moisture sources and sinks that affect an air parcel's water vapor content on its way to the target region are of minor importance. Most importantly, different from what one might expect, the strong mid-tropospheric moistening in the TTE experiment is not a direct consequence of enhanced vertical turbulent mixing that moistens air parcels as they are transported from source to target regions. Instead, it must be explained by changes in the properties of source and/or target regions themselves, which we will investigate further in later sections. Similarly, one might expect that the moistening in the $2\Delta z$ experiment with coarser vertical resolution results from enhanced numerical diffusion during vertical advection after last condensation. However, the moistening is at least partly reproduced by the Lagrangian reconstructions, which do not account for changes in nu-

merical diffusion after last condensation. Having said this, the reconstructions do not fully capture the strong moistening of dry regions, which is also evident from the positive residual term (Figure 6d). Hence, a part of the moistening might well be explained by enhanced numerical diffusion on the pathway from the source to the target point.

From the fact that the last-saturation model successfully reproduces the $\mathcal{R}$ changes between experiments, one could also conclude that they are caused by changes in the resolved circulation and the temperature structure. This is true under the assumption that the location (and hence temperature) of last-condensation points only depends on the resolved circulation and temperature structure. However, as we will explain in Section 5.5, this assumption does not always hold.

There are exceptions, where changes in parameterized moisture sources and sinks after last condensation do play a role in changing $\mathcal{R}$. As one would expect, this mainly concerns the experiments with changes in the parameterizations of turbulence and microphysics. In the TTE experiment, turbulent moistening during advection is enhanced for dry and intermediate regimes and reduced for moist regimes. Overall, the contribution from the changing moisture sources to the total $\mathcal{R}$ change is small. The (rather weak) drying of the mid troposphere in the 2-mom experiment is mainly due to a reduction in moisture sources (Figure 6c), while the plain last-saturation reconstruction predicts almost no change (Figure 6b). Hence, the drying is caused by reduced evaporation of cloud condensate or precipitation. However, additional trajectory calculations showed that the stronger reduction in $\mathcal{R}$ in the layer between 1 km and 3 km in the 2-mom experiment (Figure 1) is to a large extent captured by the plain last-saturation model. The ratio of air parcels that have subsided from the free troposphere since last condensation to air parcels that have very recently experienced saturation during ascent increases in the 2-mom experiment, indicating that the microphysical perturbation also affects the resolved transport associated with shallow convection. This would be consistent with the microphysics limiting the depth of shallow convection as mentioned in Section 3.

The Δr term includes any changes in $\mathcal{R}_{\mathrm{ICON}}$ that are not explained by either of the two Lagrangian reconstructions (with or without moisture sources along the trajectory). As explained above, the positive Δr in the $2\Delta z$ experiment might result from an increase in numerical diffusion, which is not captured by the Lagrangian reconstruction. However, there are also a positive, albeit smaller Δr for the TTE, 2-mom and $2v_{\mathrm{ice}}$ experiments, for which we do not expect changes in numerical diffusion.

In summary, the $\mathcal{R}$ changes in our experiments are largely explained by the last-saturation model, and only slightly modulated by changes in moisture sources after last condensation. In the $2\Delta z$ experiment the part of the $\mathcal{R}$ change that cannot be explained by either of the two mechanisms is likely related to changes in numerical diffusion.

5.3 Changes in source temperature vs. changes in target temperature

The fact that $\mathcal{R}$ differences are largely explained by the last-saturation model leaves changes in the saturation specific humidity in the source regions and in the target region as possible causes (Equation 4). With a linear expansion the relative humidity change predicted by the last-saturation model can be approximated as follows:

$$\Delta\mathcal{R}_{\mathrm{lc}} \approx \frac{L_v}{R_v}\frac{\mathcal{R}_{\mathrm{lc}}}{T_{\mathrm{lc}}^2}\Delta T_{\mathrm{lc}} - \frac{L_v}{R_v}\frac{\mathcal{R}_{\mathrm{lc}}}{T_{\mathrm{t}}^2}\Delta T_{\mathrm{t}} = \Delta\mathcal{R}_{\mathrm{s}} + \Delta\mathcal{R}_{\mathrm{t}}, \tag{8}$$

where R_v is the gas constant of water vapor and L_v is the specific heat of vaporization of water. The first term $\Delta\mathcal{R}_\mathrm{s}$ corresponds to the change in $\mathcal{R}_\mathrm{lc}$ due to changes in source temperature, the second term $\Delta\mathcal{R}_\mathrm{t}$ is the change in $\mathcal{R}_\mathrm{lc}$ due to changes in target temperature. From Equation 4 there should be a third term representing changes in source pressure, which we found to be negligible compared to the temperature terms. Changes in target pressure do also not play a role since our target region is a fixed altitude region in all experiments.

$\Delta\mathcal{R}_\mathrm{s}$ and $\Delta\mathcal{R}_\mathrm{t}$ are shown in Figure 7. Their sum is a good approximation of $\Delta\mathcal{R}_\mathrm{lc}$ (not shown). The two terms tend to have opposite signs, indicating that an increase in last-condensation temperature, which increases $\mathcal{R}_\mathrm{lc}$, is typically accompanied by an increase in the target temperature, which decreases $\mathcal{R}_\mathrm{lc}$. However, $\Delta\mathcal{R}_\mathrm{s}$ overcompensates $\Delta\mathcal{R}_\mathrm{t}$ for all experiments. This is likely related to the fact that the source regions are generally located above the target regions (Figure 4c) and temperature differences between experiments increase with height (Figure 1d).

The overcompensation described above is also evident from the fact that changes in $\mathcal{R}$ (Figure 6a) follow a similar pattern as changes in last-condensation temperature ΔT_lc (Figure 8a). The 2-mom experiment is an exception, because its $\mathcal{R}$ change is controlled by a change in parameterized moisture sources after last condensation (Section 5.2). As noted already in Section 5.2, the magnitudes of $\mathcal{R}$ changes are damped towards dry regimes, although the magnitudes of ΔT_lc hardly change throughout $\mathcal{R}$-space. This is because the absolute temperature of the source regions T_lc increases from dry to moist regimes (Figure 4c). Due to the non-linear dependence of e^* on T the same temperature change results in a smaller change in e^*_lc at lower temperatures than at higher temperatures, and hence in a smaller change in $\mathcal{R}$. Thus, the robustness of $\mathcal{R}$ in dry regions is a consequence of the low water vapor concentrations in the cold source regions.

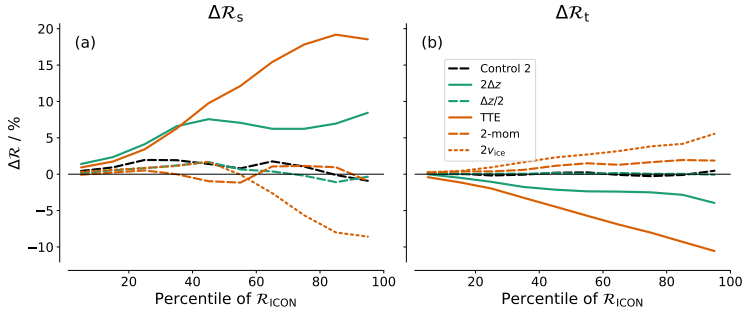

Figure 7. Contributions from source and target temperature changes to changes in mid-tropospheric $\mathcal{R}$ in the sensitivity experiments shown in $\mathcal{R}$-space. (a) Contribution from change in last-condensation temperature ($\Delta\mathcal{R}_\mathrm{s}$) and (b) contribution from change in target temperature ($\Delta\mathcal{R}_\mathrm{t}$). The sum of two terms approximates the $\mathcal{R}$ changes that were reconstructed based on the last-saturation model ($\mathcal{R}_\mathrm{lc}$ in Figure 6b). Note the different in y-axis ranges in this figure and Figure 6.

744 ### 5.4 Changes in tropical source regions vs. changes in extra-tropical source
745 regions

746 The source regions of tropical mid-tropospheric air lie both within the tropics (here
747 defined as 30°S to 30°N) and in the extra-tropics (Figure 4). Hence, changes in T_{lc} could
748 result from changes in tropical last-condensation temperatures $T_{\mathrm{lc,trop}}$, extra-tropical last-
749 condensation temperatures $T_{\mathrm{lc,extra}}$ or the share of tropical last-condensation points f:

$$\Delta T_{\mathrm{lc}} \approx f\Delta T_{\mathrm{lc,trop}} + (1-f)\Delta T_{\mathrm{lc,extra}} + \Delta f(T_{\mathrm{lc,trop}} - T_{\mathrm{lc,extra}}) \tag{9}$$

750 In moist regimes, the changes in T_{lc} are dominated by changes in $T_{\mathrm{lc,trop}}$ (Figure
751 8b), whereas in the driest 40 percentiles changes in $T_{\mathrm{lc,trop}}$ and $T_{\mathrm{lc,extra}}$ are commensu-
752 rately important (Figure 8c). Note that the fraction of tropical last-condensation events
753 f shapes the lines in Figure 8 b and c. While the absolute changes in T_{lc} are similar for
754 tropics and extra-tropics (not shown), extra-tropical changes do not affect the moist re-
755 gions because f is close to 1 there (Figure 4). Changes in f between experiments play
756 a minor role in changing T_{lc} (Figure 8d).
757

758 Internal variability (as measured by the Control 2 simulation) increases towards
759 dry regions both for tropical and extra-tropical source regions (Figure 8b,c). For the extra-
760 tropics, changes in most sensitivity experiments are similar in magnitude and go in the
761 same direction as in the Control 2 experiment, which may indicate that the control cli-
762 mate was an outlier with colder extra-tropical source temperatures. This explains why
763 in the control experiment the driest regions have a lower $\mathcal{R}$ than in all the sensitivity ex-
764 periments (Figure 6). Thus, to a large extent, changes in $T_{\mathrm{lc,extra}}$ in our sensitivity ex-
765 periments can be explained by, or at least not differentiated from, internal variability.
766 This variability is likely caused by changes in the dynamic mechanisms that bring air
767 to saturation in the extratropics and transport it to the tropics. The fact that the rel-
768 ative humidity of the dry regions is disproportionately affected by these changes empha-
769 sizes the important role of the exchange between extra-tropics and tropics in controlling
770 the humidity of the dry regions, which has been highlighted in several studies (e.g. Waugh,
771 2005; Cau et al., 2007; Roca et al., 2012; Villiger et al., 2022). In particular, a change
772 in these exchange mechanisms under warming represents a possible pathway for chang-
773 ing the relative humidity of the dry regions.
774

775 A change in $T_{\mathrm{lc,trop}}$ can generally result from a change in the tropical temperature
776 profile and/or a change in the height distribution of last-condensation points. Additional
777 analysis showed that both mechanisms are of similar importance in our experiments. De-
778 pending on the experiment they either counteract or reinforce each other. In the TTE
779 experiment, for example, tropical temperature increases (see Figure 1d) and last con-
780 densation occurs at lower altitudes on average. Both effects increase $T_{\mathrm{lc,trop}}$. In the $2v_{\mathrm{ice}}$
781 experiment, on the other hand, the two effects counteract; tropical temperature decreases,
782 but last-saturation takes place at lower altitudes on average. This explains why the $\mathcal{R}$
783 change in the $2v_{\mathrm{ice}}$ experiment is relatively small despite the large temperature change
784 (Figure 1).
785

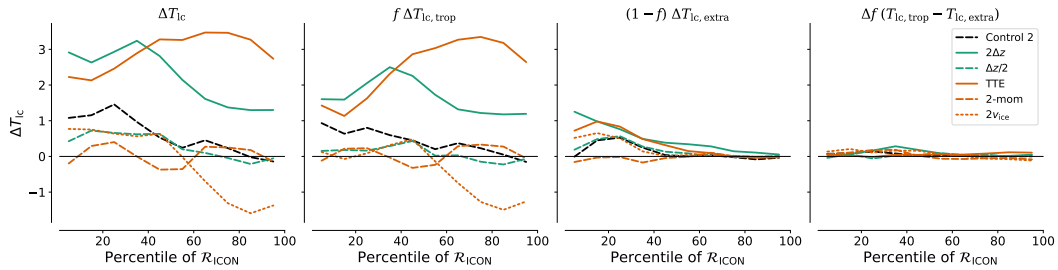

Figure 8. Changes in last-condensation temperature T_{lc} in sensitivity experiments shown in $\mathcal{R}$-space. (a) Total change of T_{lc} compared to the control experiment, (b) contribution from changes in tropical last-condensation temperatures $T_{\mathrm{lc,trop}}$, (c) contribution from changes in extra-tropical last-condensation temperatures $T_{\mathrm{lc,extratrop}}$ and (d) contribution from changes in f, the share of tropical last-condensation events.

5.5 Mechanisms behind the moistening in the TTE experiment

Mid-tropospheric $\mathcal{R}$ increases most strongly in the experiment with the TTE turbulence parameterization. The analysis above has shown that this moistening is largely explained by an increase in the average temperature at last condensation. The full distribution of tropical last-condensation temperature $T_{\mathrm{lc,trop}}$ for the control and the TTE experiment are shown in Figure 9. It is apparent that the distribution is bimodal in both experiments, implying that there are two distinct source regions for tropical mid-tropospheric air. The warm mode at around 265 K corresponds to "young" air parcels with high $\mathcal{R}$ that either experienced last condensation very recently and have since subsided over only a short distance or are even saturated at the time considered. The cold mode at around 220 K represents "old" air parcels that have subsided from the upper troposphere, where deep convection detrains preferentially, and hence end up with a low $\mathcal{R}$ in the mid troposphere. In the TTE experiment the two modes stay at roughly the same temperature as in the control experiment, but the share of young air parcels increases at the expense of old air parcels. In line with that, snapshots of $\mathcal{R}$ and moisture tendencies from microphysics reveal that condensation occurs over a broader area of the tropical mid troposphere at any given time in the TTE experiment (not shown).

One possible explanation for the broadening of saturated mid-tropospheric regions would be that convective updrafts cover a larger area. However, a corresponding analysis showed that this is not the case in the TTE experiment. The reason rather appears to be a strong turbulent mixing between lower and mid troposphere performed by the TTE scheme. Figure 10a shows vertical profiles of the specific humidity tendencies produced by the turbulence scheme in the control and TTE experiments for an exemplary model output timestep. To distinguish between different tropical large-scale circulation regimes, profiles were averaged within five 20-percentile ranges of column-integrated water vapor. In the control experiment the Smagorinsky turbulence scheme only acts within the boundary layer throughout all circulation regimes; the air within the boundary layer is moistened by mixing water vapor upward from the surface. The TTE scheme behaves very differently. Most importantly, it performs a strong mixing between the lower and mid troposphere, particularly in the moist tropics, which manifests as a drying of the lower troposphere and a moistening of the mid troposphere. In other words, the TTE scheme unintentionally acts similar to a convective parameterization.

The mid-tropospheric moistening by turbulent mixing in the TTE experiment is accompanied by increased condensation, as evident from the specific humidity tendencies produced by the microphysics parameterization shown in Figure 10b. The strong vertical mixing creates a moist background that favours condensation whenever air is displaced upward, such that condensation is not restricted to convective updrafts in the TTE experiment. This explains why the share of young air parcels with last condensation within the mid troposphere is increased.

It is worth revisiting Figure 6c, which shows how the effect of parameterized moisture sources changed compared to the control simulation. Given that the turbulent moistening of the free troposphere is more intense in the TTE experiment, it may be surprising that for the moist percentiles the moistening from parameterized processes decreased compared to the control run. However, it can be understood as a consequence of the larger share of young air parcels in the moist percentiles, for which the time period available for moistening is reduced. This is also evident from Figure 11, which shows the relative change in time since last condensation (t_{lc}) to the control experiment for all sensitivity experiments. In the TTE experiment, parcels arriving in the moistest percentile have on average been transported for a more than 40% shorter time since last condensation. For the other experiments changes in t_{lc} are within $\pm$ 10%.

While the last-saturation model technically explains the $\mathcal{R}$ increase in the TTE experiment, it does not do so for the reasons we expected. The original idea was that last-condensation points are determined by the resolved circulation and temperature structure. Thus, if the change in $\mathcal{R}$ is explained by the last-saturation model, it must be caused by changes in circulation and temperature, while changes in parameterized processes can only play a role if they affect these resolved properties. In the TTE experiment, however, condensation is not exclusively driven by resolved upward motions, but also by the strong parameterized vertical mixing of water vapor. Thus, in this case, parameterized moisture sources directly influence the location of the last-condensation events. Nevertheless, the fact that the last-saturation model succeeds in reproducing the $\mathcal{R}$ change still tells us that the change is driven by changes within the tropical source regions, i.e. the ITCZ and warm pool region, whereas changes in moisture sources during subsequent advection play a minor role.

The behavior of the TTE scheme is certainly unexpected and indicates that the scheme has not been sufficiently adapted to storm-resolving resolutions. Whether this type of one-dimensional scheme is appropriate for use at storm-resolving resolution is a question to be addressed in other studies. Having said that, the fact that even this extreme perturbation did not change $\mathcal{R}$ far beyond the inter-model spread in DYAMOND is promising. Many of the DYAMOND models used turbulence parameterizations that were not specifically adapted to storm-resolving resolution due to their early development stage. Hence, a better adaption of the schemes in future model versions might further reduce the spread in tropical $\mathcal{R}$.

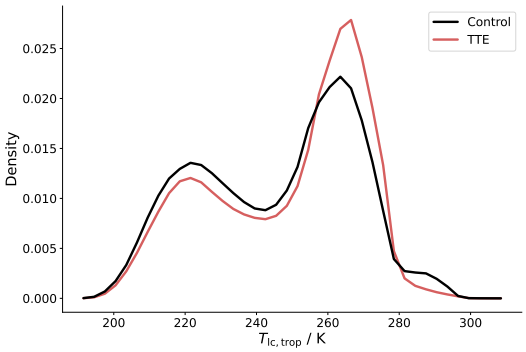

Figure 9. Probability density distribution of last-condensation temperature T_{lc} for tropical last-condensation points in the control (black) and TTE (red) experiments.

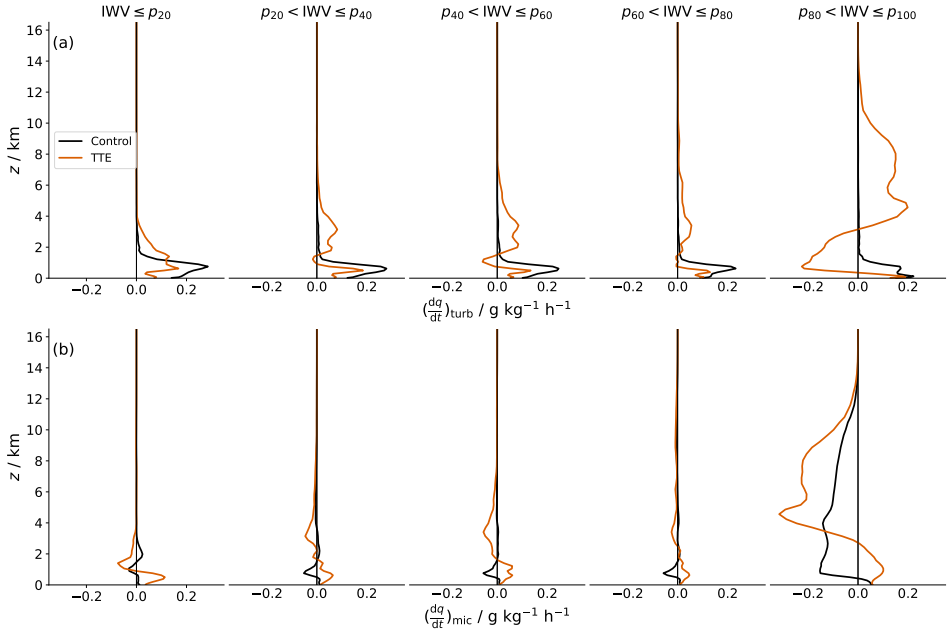

Figure 10. Moisture tendencies from (a) turbulence and (b) microphysics parameterizations in the control (black) and TTE (red) experiment for an exemplary simulation time step (17 July 2021, 12Z). Each panel in (a) and (b) shows a vertical profile of specific humidity tendencies averaged over a 20-percentile range of column-integrated water vapor, sorted from dry profiles on the left to moist profiles on the right.

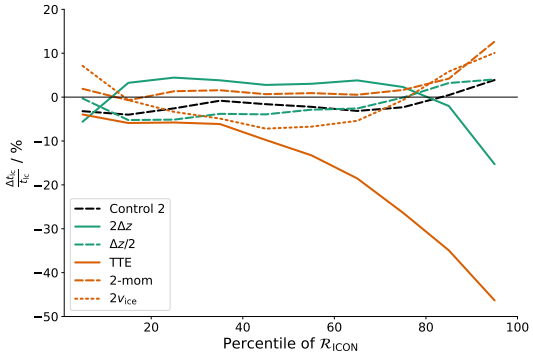

Figure 11. Relative change in time since last condensation (t_{lc}) to the control experiment for all sensitivity experiments depicted in $\mathcal{R}$-space.

6 Summary and conclusions

In this study our aim was to narrow down the model uncertainties that cause the remaining spread in tropical relative humidity $\mathcal{R}$ across GSRMs, as has been quantified in a recent study based on DYAMOND, the first model intercomparison initiative for GSRMs. To this end, we test the sensitivity of $\mathcal{R}$ to changes in model resolution and parameterizations in a series of six 45-day experiments with the ICON model in a storm-resolving configuration. The changes we apply to the model are inspired by differences among the DYAMOND models. They include changes in horizontal and vertical grid spacing, as well as in the parameterizations of microphysics and turbulence. We use a last-saturation model based on 3D backward trajectories to gain insight into the mechanisms behind the $\mathcal{R}$ changes in the sensitivity experiments. This analysis is restricted to the mid troposphere.

The rather strong perturbations applied in our sensitivity experiments result in changes in tropical $\mathcal{R}$ that are of similar magnitude as the spread across the DYAMOND models. An earlier study had shown based on the DYAMOND ensemble that the $\mathcal{R}$ spread across GSRMs is reduced compared to classical GCMs with convective parameterizations. Our experiments support this finding by showing that even strong perturbations in GSRMs cannot reproduce the spread in $\mathcal{R}$ seen in models with convective parameterizations. Moreover, our experiments show that tropical $\mathcal{R}$ is rather robust to changes in model resolution within the general scale of GSRM resolutions. The three experiments with different vertical grid spacing (800 m, 400 m and 200 m in the free troposphere) show that $\mathcal{R}$ changes are modest as soon as a certain threshold vertical resolution is exceeded. The experiments with 5 km and 2.5 km horizontal grid spacing produce a very similar $\mathcal{R}$ distribution. While these results suggest that differences in model resolution do not contribute significantly to the current $\mathcal{R}$ spread across GSRMs, it does not exclude the possibility that reducing the horizontal grid spacing to much finer scales (on the order of 200 m) could make a difference, which needs to be tested in future experiments.

In our experiments, $\mathcal{R}$ changes more strongly in response to exchanging the microphysics and turbulence schemes, indicating that the model physics rather than resolution (at storm-resolving scales) are the major source of $\mathcal{R}$ spread across GSRMs. While microphysical changes affect $\mathcal{R}$ most strongly in the altitude layer associated with shallow clouds, exchanging the turbulence scheme changes $\mathcal{R}$ over a broad altitude region in the lower to mid troposphere. We could not test the extent to which the dynamical core, and choices it makes in how to solve the transport equations, systematically influ-

ences the distribution of source regions. However, the similarity of spread between our (parameterized) physics sensitivity studies, and the relatively modest effect of grid spacing lead us to believe that these effects are unlikely large.

Like the $\mathcal{R}$ differences between DYAMOND models, the $\mathcal{R}$ changes in our experiments are smallest in the dry subsidence regimes of the tropics. This is a consequence of the low water vapor concentrations in their cold source regions. However, since the sensitivity of OLR to changes in relative humidity is particularly high in dry background states (e.g. Spencer & Braswell, 1997), small $\mathcal{R}$ differences in the dry zones are nevertheless important from a radiative perspective (Lang et al., 2021). At the same time, this study highlights that understanding humidity differences between models is particularly challenging for the dry regions. The $\mathcal{R}$ of the dry regions is subject to larger internal variability on timescales of days to months, which storm-resolving simulations are currently limited to. This is because the source regions of dry air are located remotely (mainly on the edges of the inner-tropical deep-convective regimes and in the extra-tropics) and therefore depend on the large-scale circulation. Thus, while one simulated month is sufficient to quantify systematic $\mathcal{R}$ differences in moist regions, longer simulations would increase our confidence in the sources of variability in the dry regions. Because changes in both tropical and extra-tropical origins need to be considered to understand $\mathcal{R}$ differences in dry regions (see also Cau et al., 2007; Roca et al., 2012), changes in the mechanisms of exchange between tropics and extra-tropics in a warmer climate represent an important pathway for changing the relative humidity of the dry regions, which would have important implications for the clear-sky climate feedback.

The mid-tropospheric $\mathcal{R}$ changes in our experiments, including the strong moistening in the experiment with the exchanged turbulence scheme, are largely captured by the last-saturation model. This means that most $\mathcal{R}$ changes are explained by changes in source temperature, i.e. the temperature at which air parcels typically experience last condensation, whereas changes in the moistening or drying by parameterized processes after last condensation play a minor role. This is even true when the parameterized moisture sources are modified directly, like in our microphysics and turbulence experiments. Overall, this study shows that the last-saturation model is not only successful in explaining variations in tropical $\mathcal{R}$ in the real atmosphere or a given model, as shown by many previous studies (e.g. Sherwood, 1996; Pierrehumbert & Roca, 1998; Dessler & Sherwood, 2000), but it can also be a helpful tool for explaining the causes of humidity differences between models. However, it has also become clear that last-saturation statistics can be directly affected by changes in parameterized moisture sources, e.g. by enhanced turbulent moistening. Therefore, if the last-saturation model explains a change in $\mathcal{R}$, it does not necessarily mean that it is due to changes in the resolved circulation or the temperature structure.

In our experiments the most substantial change in $\mathcal{R}$ was found in response to changing the turbulence parameterization from a Smagorinsky-type scheme to a total turbulent energy (TTE) scheme. The resulting increase in $\mathcal{R}$ was largest in the mid troposphere of moist regions. The reason appears to be that the TTE scheme produces a strong turbulent moistening of the mid troposphere in the inner, moist tropics. This moistening favours condensation, which is why from a last-saturation perspective the share of young air parcels with warm source temperatures increases in the TTE experiment. Thus, the $\mathcal{R}$ of the moist tropical regions, while less radiatively important than the dry regions, is disproportionally sensitive to vertical mixing processes that structure the humidity through their effect on the last-saturation temperatures, i.e. by increasing mid-level cloudiness, rather than their effect on the evolution of humidity since its last-saturation.

While the behavior of the TTE scheme is certainly unexpected and indicates that the scheme is poorly adapted to storm-resolving resolutions, the fact that even this extreme perturbation does not change $\mathcal{R}$ beyond the differences in the DYAMOND ensemble is very promising. Due to their early development stage, many of the DYAMOND models in fact used turbulence parameterizations that were not specifically adjusted to storm-resolving resolution. This nourishes hopes that tropical relative humidity will become even more consistent across future model versions with better adapted schemes.

7 Open Research

The ICON model code is available on `https://mpimet.mpg.de/en/science/modeling-with-icon/code-availability`.

The simulation runscripts and the code producing the plots from post-processed model output and trajectories is available on Zenodo through `https://doi.org/10.5281/zenodo.7120534`.

Acknowledgments

This research was funded by the Deutsche Forschungsgemeinschaft (DFG, German Research Foundation) under Germany's Excellence Strategy – EXC 2037 'CLICCS - Climate, Climatic Change, and Society' – Project Number: 390683824, contribution to the Center for Earth System Research and Sustainability (CEN) of Universität Hamburg.

References

Aemisegger, F., Vogel, R., Graf, P., Dahinden, F., Villiger, L., Jansen, F., ... Wernli, H. (2021, mar). How rossby wave breaking modulates the water cycle in the north atlantic trade wind region. *Weather and Climate Dynamics*, *2*(1), 281–309. doi: 10.5194/wcd-2-281-2021

Baldauf, M., Seifert, A., Förstner, J., Majewski, D., Raschendorfer, M., & Reinhardt, T. (2011, dec). Operational convective-scale numerical weather prediction with the COSMO model: Description and sensitivities. *Monthly Weather Review*, *139*(12), 3887–3905. doi: 10.1175/MWR-D-10-05013.1

Bony, S., Colman, R., Kattsov, V., Allan, R., Bretherton, C., Dufresne, J.-L., ... Webb, M. (2006, aug). How well do we understand and evaluate climate change feedback processes? *Journal of Climate*, *19*(15), 3445–3482. doi: 10.1175/JCLI3819.1

Bourdin, S., Kluft, L., & Stevens, B. (2021, apr). Dependence of climate sensitivity on the given distribution of relative humidity. *Geophysical Research Letters*. doi: https://doi.org/10.1029/2021GL092462

Bryan, G. H., Wyngaard, J. C., & Fritsch, J. M. (2003). Resolution requirements for the simulation of deep moist convection. *Monthly Weather Review*, *131*(10), 2394–2416. doi: 10.1175/1520-0493(2003)131⟨2394:RRFTSO⟩2.0.CO;2

Cau, P., Methven, J., & Hoskins, B. (2007, jun). Origins of dry air in the tropics and subtropics. *Journal of Climate*, *20*(12), 2745–2759. doi: 10.1175/JCLI4176.1

Dessler, A., & Sherwood, S. (2000). Simulations of tropical upper tropospheric humidity. *Journal of Geophysical Research*, *105*(D15), 20155–20163. doi: 10.1029/2000JD900231

Dipankar, A., Stevens, B., Heinze, R., Moseley, C., Zängl, G., Giorgetta, M., & Brdar, S. (2015, jul). Large eddy simulation using the general circulation model ICON. *Journal of Advances in Modeling Earth Systems*, *7*(3), 963–986. doi: 10.1002/2015MS000431

ECMWF. (2018). Ifs documentation cy45r1. In (chap. Part IV : Physical processes). Retrieved from `https://www.ecmwf.int/node/18714`

Held, I., & Shell, K. (2012). Using relative humidity as a state variable in climate feedback analysis. *Journal of Climate*, *25*(8), 2578–2582. doi: 10.1175/JCLI-D-11-00721.1

Held, I., & Soden, B. (2000). Water vapour feedback and global warming. *Annual Review of Energy and the Environment*, *25*(1), 441–475. doi: 10.1146/annurev.energy.25.1.441

Heymsfield, A. J., & Donner, L. J. (1990, aug). A scheme for parameterizing ice-cloud water content in general circulation models. *Journal of the Atmospheric Sciences*, *47*(15), 1865–1877. doi: 10.1175/1520-0469(1990)047⟨1865:ASFPIC⟩2.0.CO;2

Hohenegger, C., Korn, P., Linardakis, L., Redler, R., Schnur, R., Adamidis, P., ... Stevens, B. (2022, jul). ICON-sapphire: simulating the components of the earth system and their interactions at kilometer and subkilometer scales. doi: 10.5194/gmd-2022-171

John, V. O., & Soden, B. J. (2007). Temperature and humidity biases in global climate models and their impact on climate feedbacks. *Geophysical Research Letters*, *34*(18), L18704. doi: 10.1029/2007GL030429

Kluft, L., Dacie, S., Buehler, S. A., Schmidt, H., & Stevens, B. (2019, nov). Re-examining the first climate models: Climate sensitivity of a modern radiative–convective equilibrium model. *Journal of Climate*, *32*(23), 8111–8125. doi: 10.1175/JCLI-D-18-0774.1

Lang, T., Naumann, A. K., Stevens, B., & Buehler, S. A. (2021, nov). Tropical free-tropospheric humidity differences and their effect on the clear-sky radia-

tion budget in global storm-resolving models. *Journal of Advances in Modeling Earth Systems*, *13*(11). doi: 10.1029/2021MS002514

Lilly, D. K. (1962, jan). On the numerical simulation of buoyant convection. *Tellus*, *14*(2), 148–172. doi: 10.3402/tellusa.v14i2.9537

Lilly, D. K. (1967). The representation of small-scale turbulence in numerical simulation experiments. In H. H. Goldstine (Ed.), *IBM scientifc computing symposium on environmental sciences* (pp. 195–210). Yorktown Heights, New York.

Mapes, B. (2001). Water's two height scales: The moist adiabat and the radiative troposphere. *Quaterly Journal of the Royal Meteorological Society*, *127*(577), 2353–2366. doi: 10.1002/qj.49712757708

Mauritsen, T., Redler, R., Esch, M., Stevens, B., Hohenegger, C., Klocke, D., ... Schnur, R. (2022, may). Early development and tuning of a global coupled cloud resolving model, and its fast response to increasing CO2. doi: 10.31223/X5T933

Mauritsen, T., Svensson, G., Zilitinkevich, S. S., Esau, I., Enger, L., & Grisogono, B. (2007, feb). A total turbulent energy closure model for neutrally and stably stratified atmospheric boundary layers. *Journal of the Atmospheric Sciences*, *64*(2), 645–655. doi: 10.1175/2007jas2294.1

McKim, B. A., Jeevanjee, N., & Vallis, G. K. (2021, sep). Joint dependence of longwave feedback on surface temperature and relative humidity. *Geophysical Research Letters*, *48*(18). doi: 10.1029/2021GL094074

Miltenberger, A. K., Pfahl, S., & Wernli, H. (2013, nov). An online trajectory module (version 1.0) for the nonhydrostatic numerical weather prediction model COSMO. *Geoscientific Model Development*, *6*(6), 1989–2004. doi: 10.5194/gmd-6-1989-2013

Morrison, H., Curry, J. A., & Khvorostyanov, V. I. (2005, jun). A new double-moment microphysics parameterization for application in cloud and climate models. part i: Description. *Journal of the Atmospheric Sciences*, *62*(6), 1665–1677. doi: 10.1175/JAS3446.1

Phillips, V. T. J., Donner, L. J., & Garner, S. T. (2007, mar). Nucleation processes in deep convection simulated by a cloud-system-resolving model with double-moment bulk microphysics. *Journal of the Atmospheric Sciences*, *64*(3), 738–761. doi: 10.1175/JAS3869.1

Pierrehumbert, R., & Roca, R. (1998). Evidence for control of atlantic subtropical humidity by large scale advection. *Geophysical Research Letters*, *25*(24), 4537–4540. doi: 10.1029/1998GL900203

Pincus, R., Mlawer, E. J., & Delamere, J. S. (2019, oct). Balancing accuracy, efficiency, and flexibility in radiation calculations for dynamical models. *Journal of Advances in Modeling Earth Systems*, *11*(10), 3074–3089. doi: 10.1029/2019MS001621

Po-Chedley, S., Zelinka, M., Jeevanjee, N., Thorsen, T., & Santer, B. (2019). Climatology explains intermodel spread in tropical upper tropospheric cloud and relative humidity response to greenhouse warming. *Geophysical Research Letters*, *46*(22), 13399–13409. doi: 10.1029/2019GL084786

Raddatz, T. J., Reick, C. H., Knorr, W., Kattge, J., Roeckner, E., Schnur, R., ... Jungclaus, J. (2007, apr). Will the tropical land biosphere dominate the climate–carbon cycle feedback during the twenty-first century? *Climate Dynamics*, *29*(6), 565–574. doi: 10.1007/s00382-007-0247-8

Roca, R., Guzman, R., Lemond, J., Meijer, J., Picon, L., & Brogniez, H. (2012). Tropical and extra-tropical influences on the distribution of free tropospheric humidity over the intertropical belt. *Surveys in Geophysics*, *33*, 565–583. doi: 10.1007/s10712-011-9169-4

Romps, D. (2014, sep). An analytical model for tropical relative humidity. *Journal of Climate*, *27*(19), 7432–7449. doi: 10.1175/JCLI-D-14-00255.1

Ryoo, J.-M., Igusa, T., & Waugh, D. (2009, jun). PDFs of tropical tropospheric humidity: Measurements and theory. *Journal of Climate*, *22*(12), 3357–3373. doi: 10.1175/2008JCLI2747.1

Satoh, M., Stevens, B., Judt, F., Khairoutdinov, M., Lin, S.-J., Putman, W., & Düben, P. (2019). Global cloud-resolving models. *Current Climate Change Reports*, *5*(3), 172–184. doi: 10.1007/s40641-019-00131-0

Seifert, A., & Beheng, K. D. (2001, oct). A double-moment parameterization for simulating autoconversion, accretion and selfcollection. *Atmospheric Research*, *59-60*, 265–281. doi: 10.1016/S0169-8095(01)00126-0

Sherwood, S. (1996). Maintainance of the free-tropospheric tropical water vapor distribution. part ii: Simulation by large-scale advection. *Journal of Climate*, *9*(11), 2919–2934. doi: 10.1175/1520-0442(1996)009⟨2919:MOTFTT⟩2.0.CO;2

Sherwood, S., Roca, R., Meckwerth, T., & Andronova, N. (2010). Tropospheric water vapor, convection and climate. *Reviews of Geophysics*, *48*, RG2001. doi: 10.1029/2009RG000301

Smagorinsky, J. (1963, mar). General circulation experiments with the primitive equations. *Monthly Weather Review*, *91*(3), 99–164. doi: 10.1175/1520-0493(1963)091⟨0099:GCEWTP⟩2.3.CO;2

Spencer, R., & Braswell, W. (1997). How dry is the tropical free troposphere? implications for global warming theory. *Bulletin of the American Meteorological Society*, *78*(6), 1097–1106. doi: 10.1175/1520-0477(1997)078⟨1097:hdittf⟩2.0.co;2

Sprenger, M., & Wernli, H. (2015, aug). The LAGRANTO lagrangian analysis tool – version 2.0. *Geoscientific Model Development*, *8*(8), 2569–2586. doi: 10.5194/gmd-8-2569-2015

Stevens, B., Satoh, M., Auger, L., Biercamp, J., Bretherton, C. S., Chen, X., ... Zhou, L. (2019). DYAMOND: the DYnamics of the atmospheric general circulation modeled on non-hydrostatic domains. *Progress in Earth and Planetary Science*, *6*(1). doi: 10.1186/s40645-019-0304-z

Stevens, B., & Seifert, A. (2008). Understanding macrophysical outcomes of microphysical choices in simulations of shallow cumulus convection. *Journal of the Meteorological Society of Japan*, *86A*, 143–162. doi: 10.2151/jmsj.86A.143

Vial, J., Dufresne, J.-L., & Bony, S. (2013). On the interpretation of inter-model spread in CMIP5 climate sensitivity estimates. *Climate Dynamics*, *41*(11-12), 3339–3362. doi: 10.1007/s00382-013-1725-9

Villiger, L., Wernli, H., Boettcher, M., Hagen, M., & Aemisegger, F. (2022, jan). Lagrangian formation pathways of moist anomalies in the trade-wind region during the dry season: two case studies from EUREC&ampltsup&ampgt4&amplt/sup&ampgta. *Weather and Climate Dynamics*, *3*(1), 59–88. doi: 10.5194/wcd-3-59-2022

Waugh, D. W. (2005). Impact of potential vorticity intrusions on subtropical upper tropospheric humidity. *Journal of Geophysical Research*, *110*(D11). doi: 10.1029/2004JD005664

Wernli, H., & Davies, H. C. (1997, jan). A lagrangian-based analysis of extratropical cyclones. i: The method and some applications. *Quarterly Journal of the Royal Meteorological Society*, *123*(538), 467–489. doi: 10.1002/qj.49712353811

Zhang, C., Mapes, B., & Soden, B. (2003, oct). Bimodality in tropical water vapour. *Quarterly Journal of the Royal Meteorological Society*, *129*(594), 2847–2866. doi: 10.1256/qj.02.166

Zängl, G., Reinert, D., Rípodas, P., & Baldauf, M. (2015, jun). The ICON (ICOsahedral non-hydrostatic) modelling framework of DWD and MPI-m: Description of the non-hydrostatic dynamical core. *Quarterly Journal of the Royal Meteorological Society*, *141*(687), 563–579. doi: 10.1002/qj.2378